EPJ Web of Conferences **26**, 01032 (2012)
DOI: 10.1051/epjconf/20122601032

The effects of axial length on the fracture and fragmentation of expanding rings

D.R. Jones[1,a], D.E. Eakins[1], A.S. Savinykh[2], and S.V. Razorenov[2]

[1] *Institute of Shock Physics, Imperial College London, Prince Consort Road, London, SW7 2BP, UK*
[2] *Institute of Problems of Chemical Physics, Russian Academy of Sciences, Chernogolovka, Moscow Region 142432, Russia*

Abstract. Rings of Ti-6Al-4V with aspect ratios (wall thickness:axial length) of 1 : 1, 1 : 2 and 1 : 4 have been expanded to failure at radial strain rates $\dot{\varepsilon}_r \sim 1 \times 10^4\,\mathrm{s}^{-1}$ using 4340 (EN24T) steel and Cu-ETP cylindrical drivers containing a column of RDX. Expansion velocity was measured using VISAR enabling calculation of the stress-strain history of the ring alongside fragment recovery with up to 98% original ring mass recovered. Using the recovered samples average fragment length and mass and final strain have been measured along with analysis of the fracture sites to determine the active failure mechanisms. Perfect rings (aspect ratio 1 : 1) were found to undergo necking before failure, whereas the longer rings failed though ductile tensile cracking at 45° to the radius. This data is then compared with finite element analysis results.

1 Introduction

Dynamic fracture and fragmentation are late-stage processes that can occur in shock and high strain rate events. Fracture behaviour/mode is governed by the material properties, experimental variables (temperature, sample orientation etc.) and the loading history. Some materials fail catastrophically with very little deformation – brittle fracture, seen in glasses, ceramics and some metals. Most metals can accommodate some plastic strain before failure – necking followed by ductile fracture. Cracks can form along grain boundaries, through grains, through void nucleation and along shear bands. The type of fracture has a large effect on the fragments produced. Investigation of the causes of different fracture modes necessitates control of the stress state and conditions in a sample.

Expanding rings and cylinders have been studied since the 1940s using military ordnance by Taylor [1] and Gurney [2] looking at the onset of cracking and the bomb casing's radial velocity as a function of explosive mass respectively. Mott produced a seminal piece [3] on predicting the average length of fragments based on the theory of a *Mott release wave*. These propagate from fracture sites reducing stress to zero and therefore arresting any further straining or fracture in the regions they traverse, setting a minimum fragment length. Mott also noted than many fragments had edges at 45° to the radius – a sign of failure along shear bands. A large and influential body of work on fracture and fragmentation has been produced by Grady, working with Kipp. Models have been developed that consider the energy required during ductile fracture [4] and shear fracture [5]. More recent work [6] has been on combining Mott's statistical theories with Grady's energy-based ones. This resulted in a model where below a certain strain rate, the number of fractures is governed by a statistical distribution of seeding sites which all become fractures. Over this strain rate the number is restricted by the energy available for fracture.

Rings and cylinders have been driven into expansion using explosives [7], electro-magnetic coils [8] and gas guns [9] at radial strain rates $10^2\,\mathrm{s}^{-1} \leq \dot{\varepsilon}_r \leq 10^5\,\mathrm{s}^{-1}$. The symmetry of a ring experiment means that any fracture is not biased by problems arising from wave propagation found in other high strain rate tensile tests. If the ring is launched into free expansion then a record of the radial velocity (deceleration) can be used to calculate the stress-strain response of the material.

2 Methodology

2.1 Aims

The main aim of this work was to investigate the influence of stress triaxiality on the mechanisms of failure and fracture in Ti-6Al-4V (6% wt. Al, 4% wt. V, hereafter called Ti64). Ti64 was selected due to its susceptibility to failure through cracks forming along adiabatic shear bands [10] under plane strain conditions. This is due to its poor thermal conductivity; plastic deformation along the planes of maximum shear generates heat. If the heat generated can not dissipate from the shear band into the surrounding material then thermal softening outweighs work hardening leading to a flow instability [11].

The stress state during expansion was controlled by adjusting the aspect ratio of the sample ring's wall thickness to axial length. The aspect ratio was set at 1 : 1, 1 : 2 and 1 : 4 using a 3 mm wall thickness for all experiments. A perfect ring (1 : 1) is in a state of uniaxial stress once in free expansion where cylinders tend towards plane strain [12]. Driving all experiments at a strain rate of $\sim 10^4\,\mathrm{s}^{-1}$ and measuring radial velocity alongside fragment recovery and analysis would provide sufficient data for comparison of strain rate, stress-strain and strain at failure calculation alongside fragment statistics to compare with theoretical values. Post-mortem examination of the fragments would provide insight into the dominant failure mode for each

[a] e-mail: dj06@imperial.ac.uk

Table 1. Summary of experimental results.

Expt.	Ring Length (*mm*)	$\dot{\varepsilon}_r^{peak}$ (s^{-1})	ε_r^{final} (%)	% Mass Recovered	# Fragments	$\bar{m}_{frag}$ (*g*)	$\bar{l}_{frag}$ (*mm*)
A	12	1.25×10^4	26.53	60.94	9	1.57	13.19
B	6	1.10×10^4	12.24	79.20	12	0.76	13.94
C	12	1.08×10^4	29.38	98.01	8	2.83	22.52
D	Three 3 mm rings	1.36×10^4	35.70	88.24	20 (3 Rings)	0.75	24.45

stress state, as well as any pre-fracture damage accumulation such as void nucleation or adiabatic shearing.

2.2 Experimental setup and materials

The experimental setup is a development of the one used by Hoggatt and Recht [13]. Rings of Ti-6Al-4V were machined from extruded rod stock to a final outside diameter of 49 mm and a wall thickness of 3 mm. Ring lengths (axial) were 3 mm, 6 mm and 12 mm.

These sample rings were designed to be a light press fit over a driver cylinder which contains the explosive material and are located at the midpoint of the driver axis by a small lip. Originally the driver was designed and made using 4340 (EN24T) steel, however the driver material was changed to investigate different loading paths and rates for the sample ring. The driver material was changed to copper (99.9% pure: Russian grade M1, EU equivalent Cu-ETP) with a smaller diameter explosive charge. Driver length was 60 mm, with the explosive running through the entire length along the axis. Explosive diameter was 20 mm for the steel and 10 mm for the copper drivers. The explosive used in all experiments was RDX, pressed to a density of $1.6\,g\,cm^{-3}$. Total mass used in the steel driver was 50 g, compared to the copper design with 8.5 g. Detonation was initiated from both ends simultaneously using low jitter detonators.

The driver and ring combination were mounted with the axis horizontally, supported by a wooden frame at both ends in a way that would not impede expansion of the driver and sample ring. Radial velocity was measured using VISAR [14], focused on the midpoint of the ring, and on the middle ring in the case of three rings. The oscilloscope used to record the VISAR data was triggered using ionising strips oriented along the length of the RDX charge. A summary of the experiments is given in Table 1. Experiment A was the only one to use the 4340 steel driver. In each case one Ti64 ring was used, except experiment D where three 3 mm rings were stacked at the centre of the driver axis to increase the chances of significant fragment recovery. A section of each ring was lightly sanded to provide a diffusely reflecting surface for the VISAR.

2.3 Modelling approach

Hydrocode simulations of the copper driver experiments were performed using ANSYS Autodyn. Both 2d (axial symmetry) and 3D (quarter symmetry) models were simulated using a Lagrangian mesh. Equation of State for both the copper and Ti64 was a $U_s - u_p$ model. A piecewise Johnson-Cook strength model was used for the copper, and Steinberg Guinan for the Ti64. The RDX used a JWL EoS. After a mesh convergence study the mesh for the ring(s) was set as $50\,\mu$m. Gauges were placed along the outer surface of the ring to compare directly with VISAR free surface velocity data.

3 Results

Strain and strain rate were calculated using equations (1) and (2) respectively [13],

$$\varepsilon_r = ln\frac{r}{r_0} \tag{1}$$

$$\dot{\varepsilon}_r(t) = \frac{\dot{r}(t)}{r(t)} \tag{2}$$

where the outer radius of the ring is represented by r, with r_0 being the initial outer radius. The VISAR diagnostic measures free surface velocity v_{fs} which is approximately double the radial velocity $\dot{r}$. Due to the reflective surface being curved and twisting of the ring during expansion defocusing and misalignment of the system resulted in velocity time histories being shorter than desired as the signal intensity degraded at late time. Peak radial strain rate $\dot{\varepsilon}_r^{peak}$ is calculated using the maximum radial velocity. Average radial strain rate will be lower than this value – see the velocity profiles in Sections 3.1 & 3.2. In all experiments radial strain rate $\dot{\varepsilon}_r$ was on the order of $10^4\,s^{-1}$. Fragment recovery was typically above 60% wt., with up to 98% in some cases. Final radial strain ε_r^{final} is calculated from measuring the outer radius of recovered fragments. Note this is not equivalent to strain at failure as the fragments will continue to deform until the release waves from the fracture sites at each end have traversed the entire fragment. Measurement of strain at failure is challenging as it requires high-speed imaging of both the outer and inner surfaces of the ring during the expansion process. A common method for cylinders directly driven by explosives is observation of the release of explosive products through the cylinder wall [15].

3.1 4340 steel Driver – 12 mm ring

Experiment A used a 12 mm ring with a 4340 steel driver (bottom, Figure 1). The VISAR profile is shown in Figure 2. It is clear that the ring experiences multi-step loading before it reaches peak radial velocity with an overall rise-time of 550 ns. This could be due to interactions of stress waves, i.e. reflection of the elastic precursor from the outer face of the driver interfering with a following shock

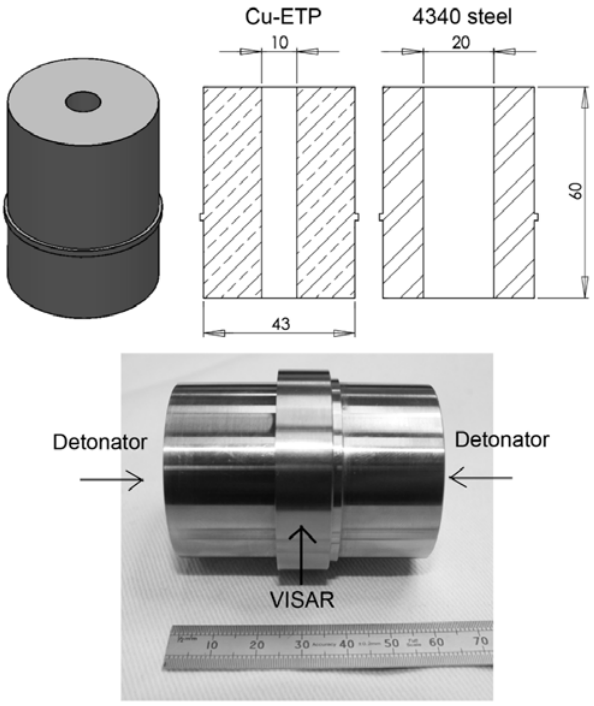

Fig. 1. *Top:* Dimensions of the copper *(left)* and steel *(right)* drivers. *Bottom:* Steel driver & 12 mm Ti64 ring.

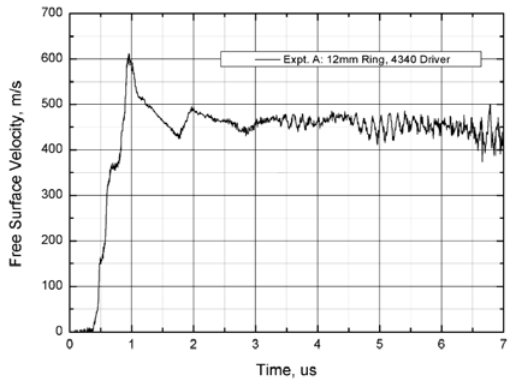

Fig. 2. Free surface velocity profile for Expt. A (12mm Ring, 4340 steel Driver).

coming from the inner face. The time between steps is too short to be simple reverberation of the initial shock wave. It could also be due to a phase change or failure in the driver; the steel fragments had evidence of fracture through shear banding. The Chapman-Jouget pressure in RDX at $1.6\,\mathrm{g\,cm^{-3}}$ is 28.3 GPa [16], well in excess of the $\alpha - \varepsilon$ phase transition in 4340 steel at ~13 GPa [17].

Failure was almost exclusively through cracks at 45° to the radius. Examination of the fragments after polishing and etching suggests the cracks are a result of ductile tensile failure along the planes of maximum shear. Fragments had a slightly 'barrelled' cross section with the axial centre of the ring experiencing more radial strain than the two ends. Average fragment length was much smaller than the other 12 mm experiment (C) in line with current theories that predict more fragments at higher strain rates [6].

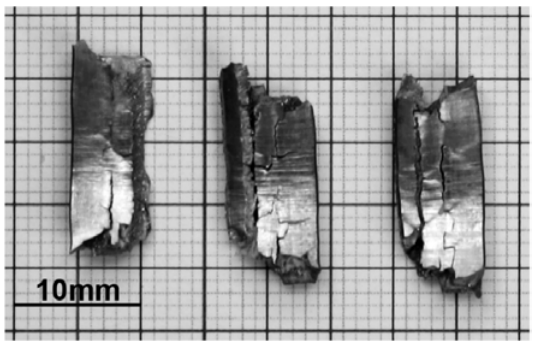

Fig. 3. Fragments (*inside surface*) from Expt. C, showing fracture along the ring circumference.

Marginal strain was observed along the ring's axis in agreement with plane strain deformation for a cylinder.

3.2 Copper driver

Subsequent experiments utilised a copper driver. It was thought that the higher ductility of copper would avoid failure in the driver. A smaller amount of RDX combined with a thicker driver wall (see Figure 1) and no phase changes would reduce the effect of stress wave interaction causing step loading. VISAR profiles are shown in Figure 6 (solid lines). Experiments B, C & D all show an elastic-plastic transition at $\sim 110\,\mathrm{m\,s^{-1}}$. It is clear that the loading of the ring is much quicker, now reaching peak velocity in $\sim 0.3\,\mu$s as opposed to $0.6\,\mu$s with the steel driver. The multi-step loading has also been greatly reduced.

3.2.1 Experiment B – 6 mm ring

Peak radial velocity was $515\,\mathrm{ms^{-1}}$. The ends of the recovered fragments were very sharp consisting again of cracks at ±45° to the radius. Interaction of many neighbouring cracks created complex jagged fragment ends. The cross section of the ring had gone from a rectangle to a trapezium with the inner surface of the ring being the base. In this case there was also fracture occurring along the ring's circumference, shown in Figure 3. These fractures typically extended through ~75% of the ring's thickness, but occasionally fully penetrated resulting in detachment from the main fragment (*left*, Fig. 3).

The average fragment length was much shorter than the other copper driver experiments, at 13.94 mm compared to around 23 mm. Theory for plane strain deformation predicts that fragment length is dictated by strain rate. It is thought that the circumferential cracking is introducing more nucleation sites for shear bands to form. Detailed images of the circumferential cracking are shown in Figure 4. These show void nucleation and coalescence in lines parallel to the cracks which are formed through void coalescence. The VISAR profile exhibits a large pull-back in velocity, from $515\,\mathrm{ms^{-1}}$ to $160\,\mathrm{ms^{-1}}$ in $0.6\,\mu$s. During this time there is release from the outer edges of the ring, which combine with the main stress wave coming up through the centre of the ring from the converging

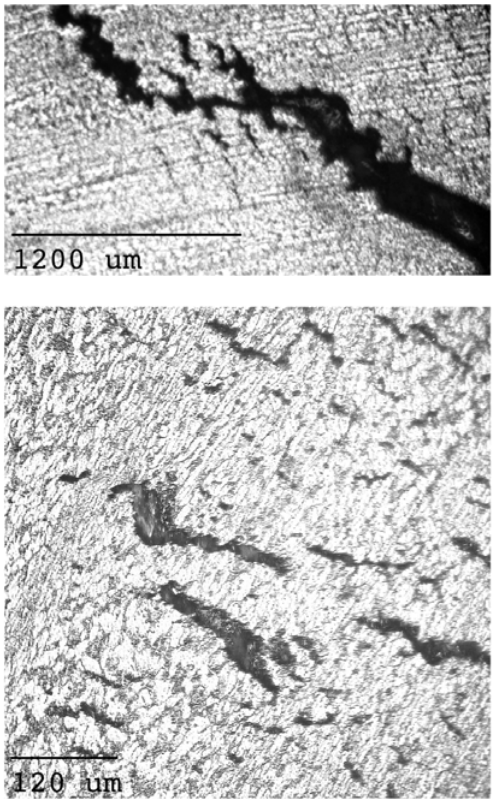

Fig. 4. Expt. B. *Top:* Detail of circumferential ductile failure, section taken left-right in Figure 3. *Bottom:* Void nucleation and coalescence.

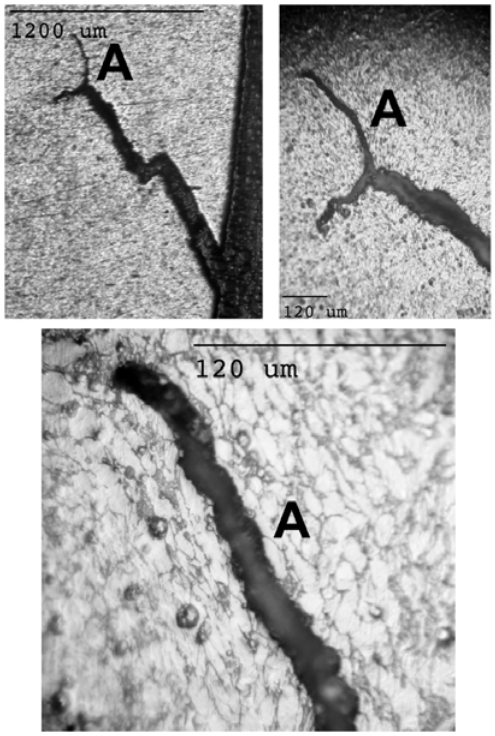

Fig. 5. Expt. C. Arrested crack from outer surface of the ring. Increasing magnification of ductile crack at A.

explosive waves in the driver. Interacting release waves and stress waves could result in spallation, creating the void nucleation and the subsequent circumferential cracks. Final radial strain was by far the lowest (12.24%) suggesting that the circumferential cracking occurred early in the expansion process, initiating premature radial failure.

3.2.2 Experiment C – 12 mm ring

Experiment C used an aspect ratio of 1 : 4. The bulk failure mode was through cracks inclined at 45° to the radius, showing signs of ductile failure along shear localisations, albeit not adiabatic. Fragments possessed a roughened inner and outer surface with bands along the ring axis. From analysis of fragments with arrested cracks it is evident that fracture initiates on the outer surface of the ring, with tensile ductile failure along lines of maximum shear. Propagating cracks had a blunt tip, shown in Figure 5. Fragment length was considerably longer than both the other 12 mm ring and the 6 mm ring. The former can be attributed to the lower strain rate, and the latter because there was no circumferential cracking seen causing damage to seed radial fracture. The VISAR record reveals a small dip and increase in radial velocity between 0.4 and 0.6 μs. This is not observed in the other copper drive experiments or the hydrocode models. It is believed that this is due to rotation of the reflecting surface as the ring expands, which is exaggerated if the VISAR probe is not precisely aligned to the middle of the ring. Fragment recovery was excellent, at 98%. This enabled full reconstruction of the ring giving more insight into fragment length and mass distribution, lengths ranging from 10 mm to 30 mm.

3.2.3 Experiment D – Three 3 mm rings

Experiment D used perfect rings, i.e. aspect ratio 1 : 1. This promotes uniaxial-stress in the ring, with hoop stress being the dominant stress component. Three rings were used to aid chances of enough fragment recovery for statistics and metallography. The peak radial velocity was higher than the other copper drive experiments, at 660 ms^{-1}. Rise time and magnitude of the velocity agrees very closely with the hydrocode models. The VISAR profile shows a pronounced ringing, with a period of $\sim 1\,\mu$s corresponding to the transit time of the reverberating stress wave through the 3 mm wall and back agreeing with the elastic wave speed in Ti64, 6.13 mm $\mu\mathrm{s}^{-1}$ [18]. The recovered fragments exhibited extensive numbers of arrested necks, with fracture sites also showing signs of necking before failure. Fracture was a mixture of cracks inclined at 45° to the radius and ductile tensile fracture in necking sites through void coalescence. No arrested cracks were observed. Average fragment length was the longest of all the experiments, at 22.45 mm, with lengths from 15 mm to 35 mm found. However, radial strain rate was the highest of all at $1.36 \times 10^4\ \mathrm{s}^{-1}$, which should result in the shortest fragments.

The necking that was only observed in this aspect ratio allows for greater accumulation of plastic deformation before fracture.

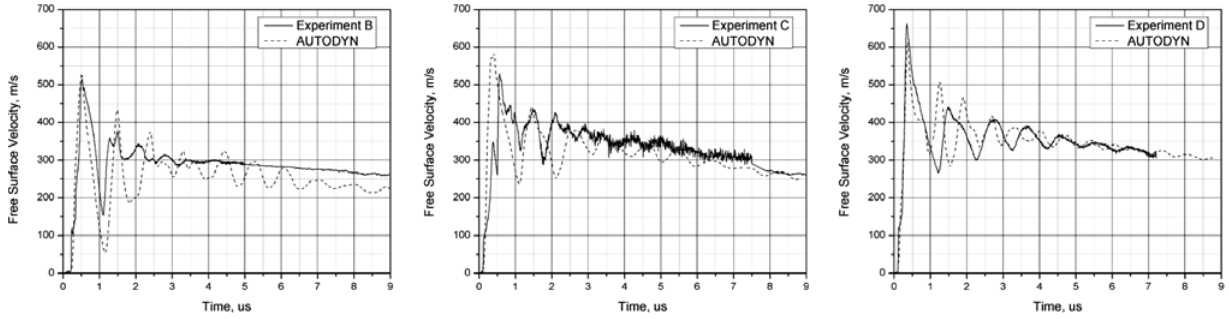

Fig. 6. Free surface velocity data (*solid line*) and simulations (*dashed*) for the copper driver experiments. *Left:* 6 mm Ring, *Centre:* 12 mm Ring, *Right:* 3 × 3 mm Rings, data from centre ring.

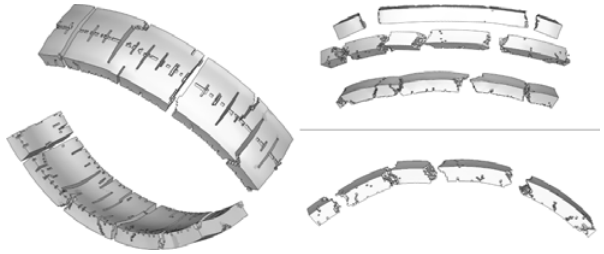

Fig. 7. 3D Simulation results. *Left:* Outer and inner surfaces of experiment C. *Right (top):* Experiment D, 3 rings. *Bottom:* Detail of centre ring.

3.3 Modelling results

The results of the 2D simulations are shown in Figure 6. In the 6 mm and 3 mm cases the rise time and magnitude of the peak radial velocity is a very close match to the data. The elastic precursor seen in the experimental data is not reproduced. The rate of deceleration in all the rings i.e. the gradient of the slope after peak velocity is also a very close fit. Whilst the models capture the general trend of the stress wave reverberating in the ring through the wall thickness, the frequency of these oscillations and the rate at which they are damped is erroneous for most of the duration.

The 3D models used a simple failure criterion in the Ti64 of failure of a node when a principal strain of 0.25 is reached. The stochastic feature was enabled to simulate flaws in the material. Results are shown in Figure 7. Fragment number is consistently higher than the experiments (expt. D model predicts 12 fragments compared to the 8 produced). The 12 mm ring is showing some signs of failure through shear banding although most fractures are ductile, due to the simple failure criteria. The 3 mm ring model shows necking followed by failure at 45° to the axis in good agreement with the recovered fragments. The arrested necks observed in the experiment are also reproduced. The circumferential fracturing seen in Experiment B was found in the model, although with the fractures going the opposite way (i.e. along the other plane of maximum stress, from the bottom edges of the ring to the outside centre as opposed to the experiment where the fractures run from top edges to bottom centre). The basic failure model used results in failed nodes at the inner edges of the ring which seed the circumferential cracks. In all cases the final cross-sectional profile of the fragments is very close to the shapes found in the experiments.

4 Conclusions

Rings of Ti6Al4V have been dynamically expanded using a cylindrical driver containing RDX, detonated at both ends simultaneously. Driver material was 4340 steel and 99.9% pure copper. This method provided axially symmetric expansion. Ring axial length was set at 3 mm, 6 mm and 12 mm for a fixed wall thickness of 3 mm, creating a different aspect ratio and stress state in each ring. Point VISAR and recovery of fragments provided data on radial velocity, fragment size, weight and the fracture mechanism.

Using the steel driver resulted in a stepped loading of the ring, with severe deformation and failure of the driver. The copper driver provided much more satisfactory loading, with a steep single pulse in the ring. Radial strain rates were between 1 to $1.4 \times 10^4\ s^{-1}$, corresponding to peak radial velocities of 500 to 660 ms^{-1}. Fragment recovery was between 60% and 98% enabling metallographic analysis of the failure modes. In perfect rings (1 : 1 aspect ratio) failure was a mix of ductile tensile fracture and ductile cracking, preceded by necking. In the rings with a longer axial length fracture was through ductile cracking on planes 45° to the radius, with little deformation surrounding the fracture sites. In the 1 : 2 aspect ratio ring extensive failure was seen along the circumference of the ring, as a result of tensile stresses arising from interacting stress waves. 2D and 3D models were used to compare radial velocity and a basic failure model used to estimate the number of fragments and distribution of cracks, with results in good agreement with the experimental data.

Future work would include more diagnostics covering radial velocity, as issues with VISAR defocusing meant only a short velocity history was recorded. Multiple point velocimetry would also help ensure that the point of interest is not on a fracture site. It could also be incorporated to analyse the loading wave into the ring by observing the driver surface. High-speed imaging would enable measurement of strain-at-failure and analysis of fracture initiation.

The author would like to thank the Institute of Problems of Chemical Physics for the opportunity, facilities and assistance for this series of experiments and Dr. Bill Proud for organising the collaboration. Also the Institute of Shock Physics technical staff for sample preparation, the Imperial College Materials department for use of their metallography workshop and AWE for funding and support.

References

1. G.I. Taylor (G.K. Batchelor editor), *The Scientific Papers of Sir Geoffrey Ingram Taylor, Volume III* (Cambridge University Press, 1963) 387-391
2. R.W. Gurney, Ballistic Research Laboratories Report **BRL-405**, 1943
3. N.F. Mott, Proc. R. Soc. A **189**, 1947 300-308
4. M.E. Kipp, D.E. Grady, J. Mech. Phys. Sol. **33, 4** 1985 399-415
5. D.E.Grady, M.E. Kipp, J. Mech. Phys. Col. **35, 1** 1987 95-119
6. D.E.Grady, M.L. Olsen, Int. J. Imp. Eng. **29** 2003 293-306
7. C.R. Hoggatt, R.F. Recht, J. Appl. Phys. **39, 3** 1978 1856-1862
8. F.I. Niordson, Exp. Mech. **5, 1** 1965 29-32
9. R.E. Winter, H.G. Prestidge, J. Mat. Sci. Lett. **13, 8** 1978 1835-1837
10. S.C. Liao, J Duffy, J. Mech. Phys. Solids **46, 11** 1998 2201-2231
11. Y. Bai, B. Dodd, *Adiabatic Shear Localization: Occurrence, Theories and Applications* (Pergamon Publishing, 1992)
12. R.H. Warnes, T.A. Duffey, R.R. Karpp, A.E. Carden, LASL Report **LA-UR-80-1543** 1980
13. C.R. Hoggatt, R.F. Recht, Exp. Mech. **9, 10** 1969 441-448
14. L.M. Barker, R.E. Hollenbach, J. Appl. Phys. **43** 1972 4669
15. T Hiroe *et al.*, Int. J. Imp. Eng. **35, 12** 2008 1578-1586
16. N.L. Coleburn, US Naval Ordnance Laboratory Report **NOLTR 64-58** 1964
17. R.E. Franz, J.L. Robitaille, US Ballistic Research Laboratory Report **ARBRL-MR-02951** 1979
18. Z Rosenberg, Y Meybar, J. Phys. D: Appl. Phys. **16** 1983